Laser-Induced Translative Hydrodynamic Mass Snapshots: Noninvasive Characterization and Predictive Modeling via Mapping at Nanoscale

X. W. Wang,[1] A. A. Kuchmizhak,[1,2,3,*] X. Li,[1] S. Juodkazis,[1,4] O. B. Vitrik,[2,3] Yu. N. Kulchin,[3] V. V. Zhakhovsky,[5,6] P. A. Danilov,[3,7] A. A. Ionin,[7] S. I. Kudryashov,[3,7,8] A. A. Rudenko,[7] and N. A. Inogamov[6,5]

[1]*Center for Micro-Photonics, Swinburne University of Technology, John Street, Hawthorn 3122, Victoria, Australia*
[2]*School of Natural Sciences, Far Eastern Federal University, Vladivostok 690041, Russia*
[3]*Institute of Automation and Control Processes, Far Eastern Branch, Russian Academy of Science, Vladivostok 690041, Russia*
[4]*Melbourne Centre for Nanofabrication, ANFF, 151 Wellington Road, Clayton VIC 3168, Australia*
[5]*Dukhov Research Institute of Automatics, ROSATOM, Moscow 127055, Russia*
[6]*Landau Institute for Theoretical Physics, Russian Academy of Sciences, Chernogolovka 142432, Russia*
[7]*Lebedev Physical Institute, Russian Academy of Sciences, Moscow 119991, Russia*
[8]*ITMO University, St. Peterburg 197101, Russia*

(Received 4 May 2017; revised manuscript received 3 August 2017; published 25 October 2017)

Subwavelength structures (meta-atoms) with artificially engineered permittivity and permeability have shown promising applications for guiding and controlling the flow of electromagnetic energy on the nanoscale. Ultrafast laser nanoprinting emerges as a promising single-step, green and flexible technology in fabricating large-area arrays of meta-atoms through the translative or ablative modification of noble-metal thin films. Ultrafast laser energy deposition in noble-metal films produces irreversible, intricate nanoscale translative mass redistributions after resolidification of the transient thermally assisted hydrodynamic melt perturbations. Such mass redistribution results in the formation of a radially symmetric frozen surface with modified hidden nanofeatures, which strongly affect the optical response harnessed in plasmonic sensing and nonlinear optical applications. Here, we demonstrate that side-view electron microscopy and ion-beam cross sections together with low-energy electron x-ray dispersion microscopy provide exact information about such three-dimensional patterns, enabling an accurate acquisition of their cross-sectional mass distributions. Such nanoscale solidified structures are theoretically modeled, considering the underlying physical processes associated with laser-induced energy absorption, electron-ion energy exchange, acoustic relaxation, and hydrodynamic flows. A theoretical approach, separating slow and fast physical processes and combining hybrid analytical two-temperature calculations, scalable molecular-dynamics simulations, and a semianalytical thin-shell model is synergistically applied. These advanced characterization approaches are required for a detailed modeling of near-field electromagnetic response and pave the way to a fully automated noninvasive in-line control of a high-throughput and large-scale laser fabrication. This theoretical modeling provides an accurate prediction of scales and topographies of the laser-fabricated meta-atoms and metasurfaces.

DOI: 10.1103/PhysRevApplied.8.044016

I. INTRODUCTION

Precise high numerical-aperture (NA) nanoscale laser ablation of thin metal films, using short and ultrashort laser pulses (full width at half-intensity maximum $\tau_L < 10$ ps), is a key enabling physical process in emerging large-scale technologies in high-throughput MHz- [1–4] or GHz-rate [5] processing of thin-film transistors [6], scribing thin-film solar cells [7], ablative fabrication, and laser-induced forward-transfer (LIFT) printing of advanced plasmonic and dielectric nanophotonic metasurfaces and circuits [8–17]. In comparison to short laser pulses ($\tau_L > 10$ ps), the ultrashort ones are broadly used during such precise ablation, holding a promise of providing an ultimate spatial resolution, despite the underlying more intense response of the electron subsystem to laser exposure with dramatically higher electron-lattice temperature (for $\tau_L < 1$ ps) and pressure gradients, resulting in intense nanoscale hydrodynamic flows and ultrafast quenching of corresponding transient melt configurations—e.g., a nanodroplet, separating from a nanojet [18].

Radial nanoscale mass distributions inside frozen center-symmetric nanostructures were previously demonstrated to be inhomogeneous with intense hydrodynamic gradient-driven melt redistributions in the melt stage and even some emerging hidden subsurface features (e.g., counterjets, cavities) [19–26]. A number of focused studies were devoted to separation dynamics of molten spherical

*alex.iacp.dvo@mail.ru

nanodroplets from a laser-induced nanojet [18] and their deposition on an acceptor substrate [27] in the context of the promising LIFT-printing technology [10]. Meanwhile, till now nano- and microscale resolidified structures on thin supported metallic films were only qualitatively or semiquantitatively visualized in terms of their internal structure by top- or side-view scanning electron microscopy (SEM), without visualization of hidden nanoelements and quantitative acquisition of their mass distribution parameters (film or membrane relief profile or metal thickness, shape, etc.). The latter parameters were demonstrated to be crucial in supporting the propagation of surface plasmon-polaritons in surface arrays of laser-induced nano- or microstructures and managing their related surface electromagnetic nodes (hot spots), important for various applications as surface-enhanced Raman scattering and photoluminescence enhancement, plasmonic coloration, and nonlinear optical applications [12,17,28]. Hence, highly informative, noninvasive quantitative nanocharacterization procedures are required for the comprehensive acquisition of mass distributions in such nanoelements of plasmonic metasurfaces produced by ultrafast laser printing (preferably via an in-line inspection).

Alternatively, molecular-dynamics (MD) and hydrodynamics (HD) simulations can potentially provide a realistic detailed description of the underlying spatiotemporal dynamics of the laser-induced nanoscale hydrodynamic flows, enlightening the corresponding physical mechanisms [26,29–31]. Specifically, several previous MD studies [32–34] considered an initial stage of fs-laser-induced separation of a thin metal film from a substrate caused by a negative pressure at the film-substrate contact boundary, while much later stages, when the formation of a central nanojet occurs, were not achieved in these simulations. Meanwhile, forming and development of multiple nanojets were simulated during two-temperature-model- (TTM) MD (TTM-MD) studies of fs-laser spallation [35]. Also, a rather complicated process of formation of subsurface voids (a nanoporous subsurface layer) on the fs-laser irradiated metal surface [20,25,36,37] is modeled, using combined theoretical approaches based on Monte Carlo–MD [20] or TTM-MD codes [25,26,33,34,38].

Despite these remarkable demonstrations of the predictive theoretical capability, a substantial detailed experimental input is usually required as a starting point for the comprehensive justification of such theoretical models and comparative quantitative verification of their results, to enable future important quantitative predictions and optimization of experimental parameters. In this work, we present experimental procedures based on the SEM inspection of nanoscale focused-ion-beam (FIB) cuts and energy-dispersive x-ray fluorescence (EDX) nanoscale profiling, for nanoscale invasive and noninvasive characterization of mass-density distributions within individual radially symmetric topological surface structures—separate nanobumps and jets on nanobumps, produced by single-shot ablation of 50-nm-thick glass-supported gold films by tightly focused fs-laser pulses at variable pulse energies. These structures are fabricated to reveal quenched configurations of melt, yielding from irreversible nanoscale translative hydrodynamic flows and nanoscale heat conduction, by means of the developed characterization procedures. By taking into account all underlying physical processes associated with laser-induced energy absorption, electron-ion energy exchange, acoustic relaxation, and hydrodynamic flows, the theoretical approach based on the separation of the slow and fast physical processes and combining hybrid analytical two-temperature calculations, scalable molecular-dynamics simulations, and the semianalytical thin-shell model is tested in terms of its predictive capabilities regarding such nanoscale resolidified morphologies.

II. EXPERIMENTAL STUDY OF NANOSCALE TRANSLATIVE MASS REDISTRIBUTIONS

To experimentally reveal the initial stage of metal film blistering from its substrate under the tightly focused fs-laser pulse irradiation, as well as to follow the subsequent evolution of the molten material through nanoscale hydrodynamic flows and quenching (resolidification) of transient nanofeatures—from the parabola-shaped nanobumps to the small nanojets, their cross-sectional cuts are prepared, using Ga^+-ion FIB milling (Raith IonLINE). To do this, an *e*-beam-evaporated 50-nm-thick Au film, covering a silica glass substrate, is first patterned with well-ordered arrays of different surface structures—smaller and larger nanobumps; with small nanojets atop for the larger fluences [Figs. 1(a)–1(e)]. The spatial period of arrays is set 2 μm.

The small structures are formed in the fluence range below the thresholds for nanojet and hole appearance [highlighted by green and red colors in Fig. 1(h), respectively]. Studying the small structures can shed light on the reasons of material redistribution during their initial formation stage, because the main governing processes, including melting, material flow, and recrystallization, are triggered at such a time scale. Additionally, these experimental results can be used to justify the previously suggested theoretical models [30,34,41,42].

For laser patterning, second-harmonic ($\lambda = 515$ nm), 230-fs FWHM laser pulses from a Yb:KGW laser system (PHAROS, Light Conversion Ltd.) are focused into a submicrometer spot using a dry objective lens with numerical aperture NA = 0.5 (Mitutoyo M Plan Apo NIR HR). Each surface structure presented in Figs. 1(a)–1(e) is produced by single-pulse irradiation, keeping the constant absorbed fluence F for each single array, while increasing its value stepwise from 26 to 47.8 mJ/cm^2 per pulse for subsequently patterned arrays [Figs. 1(a)–1(e)].

After such laser fabrication, the sample, containing nanostructures, is overcoated with a protective titanium (Ti) film. The Ti coating provides a good contrast of FIB

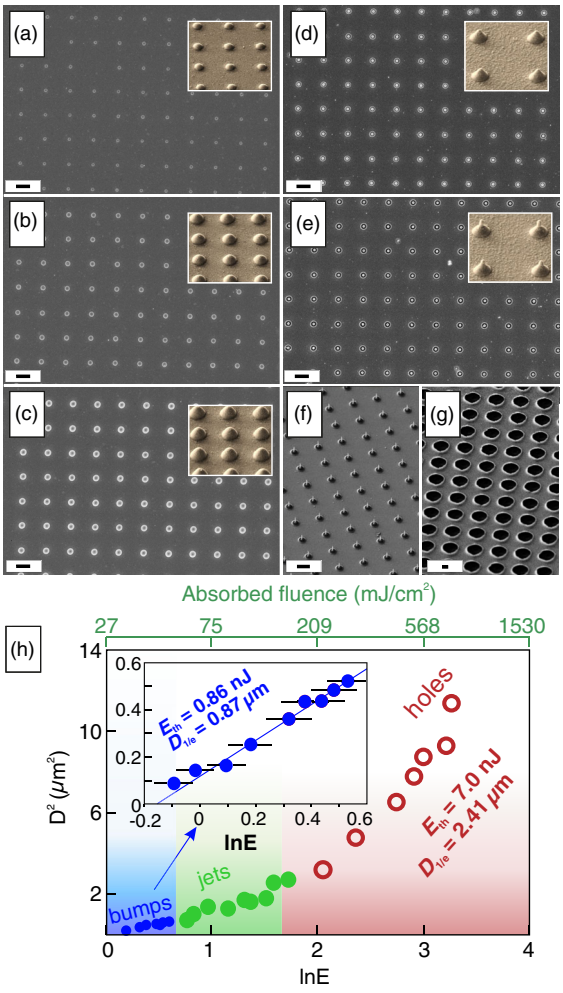

FIG. 1. (a)–(e) SEM images of the nanostructure arrays fabricated at increasing absorbed fluence in units of mJ/cm^2: (a) 26, (b) 33.6, (c) 39.4, (d) 45.2, (e) 47.8; the insets present side-view (view angle of 45°) SEM images of the corresponding structures. (f),(g) Side-view (view angle of 45°) SEM images of nanojet and microhole arrays fabricated at absorbed fluences: (f) 92 and (g) 1130 mJ/cm^2, respectively. The scale bars for these images correspond to 1 μm. The absorbed fluence is estimated as $F = AE(\pi R_{\rm opt}^2)^{-1}$ considering the constant absorbance of $A = 0.35$ [39,40] and optical spot radius $R_{\rm opt} = 0.61\lambda\ ({\rm NA})^{-1}$. (h) Squared outer diameter D^2 of the nanobumps, nanojets, and through holes versus the natural logarithm of the applied pulse energy $\ln E$ (E in nJ, bottom axis) and absorbed fluence F (upper colored axis). The inset illustrates the magnified leftmost part of this dependence. The slope of the fitting lines for bumps and through holes indicates the characteristic energy deposition diameter, while the intersection with the x axis indicates the threshold pulse energy required to produce the bump structure.

cuts of the laser-fabricated nano- and microstructures during their SEM visualization. For small parabola-shaped microbumps [Figs. 1(a) and 1(b)], the 100-nm-thick Ti film is postdeposited, while for taller structures a twice-thicker protective layer is used to ensure their complete coverage. The succeeding FIB milling of the sample is performed at the 30-kV acceleration voltage and the relatively small beam current of 50 pA to produce smooth walls. For each type of nano- or microstructure, at least ten similar cuts are prepared to provide statistical significance and to reveal small fluctuations due to the instability of the laser fluence, as well as stochastic inhomogeneities of the metal film-glass substrate. Finally, the fabricated FIB cuts are visualized, using a field-emission SEM module of the e-beam lithography writer Raith 150-TWO.

By measuring the dependence of squared diameters D^2 of the through holes produced in the Au film versus natural logarithm of incident pulse energy, $\ln(E)$, the corresponding threshold pulse energy of $E_{\rm th,hole} = 7.0 \pm 0.7$ nJ [red dots in Fig. 1(h)] is estimated, with its slope indicating the characteristic energy deposition diameter $D_{1/e,{\rm hole}}$ of 2.4 μm. This gives the deposited threshold fluence $F_{\rm th,hole} = AE_{\rm th,hole}(\pi R_{1/e,{\rm hole}}^2)^{-1} = 53 \pm 7$ mJ/cm^2 for the 50-nm-thick Au film absorbance $A \approx 0.35$ [39,40] (see also Note 3 in the Appendix), which is in good agreement with previously reported values; see also Fig. 4 below. Similar dependences of basement radii measured for nanobumps and jets [blue and green dots in Fig. 1(h)], evaluated considering the bending-inflection point on the film-membrane surface, indicate practically the same deposited fluence $F_{\rm th,bump} = AE_{\rm th,bump}(\pi R_{1/e,{\rm bump}}^2)^{-1} = 49 \pm 6$ mJ/cm^2 at the threshold pulse energy $E_{\rm th,bump} = 0.86 \pm 0.09$ nJ and almost threefold smaller energy deposition radius $D_{1/e,{\rm bump}} = 0.87 \pm 0.09$ μm. Obviously, the different energy deposition scales—$D_{1/e,{\rm bump}} \approx 0.9$ μm and $D_{1/e,{\rm hole}} \approx 2.4$ μm—indicate, for the same focusing conditions, the corresponding different temporal scales of their formation, enabling the laser-deposited energy in the thin film to be transported laterally from the focal spot (diameter $D_{\rm opt} \approx 1.2$ μm) via electronic heat conduction. Specifically, in the case of microholes $t_{\rm hole} \approx (D_{1/e,{\rm hole}}^2 - D_{\rm opt}^2)/4\chi \approx 9$ ns, respectively, for the high-temperature (1000 K) thermal diffusivity coefficient of solid gold $\chi \approx 1.2$ cm^2/s [43] being comparable to previous similar estimates [44,45].

A series of side-view SEM images [Figs. 2(a)–2(e)] demonstrate the central cross-section cuts of the different structures produced on the surface of the Au film at the increasing absorbed fluence [each presented image illustrates the cut of one of the surface structure previously shown in Figs. 1(a)–1(e)]. The detailed analysis of the cuts indicate that for parabola-shaped nanobumps produced at the pulse energies slightly above the measured threshold for the nanobump formation ($F_{\rm th} > 49$ mJ/cm^2), the thickness of the Au film remains almost unchanged with some negligible material redistribution, occurring only near the edges of the nanobump [Figs. 2(a1) and 2(b1)]. For the increasing absorbed fluence [Figs. 2(c) and 2(d)], significant thinning of the film is observed (in some specific points near the nanobump edge the film becomes twice thinner) and is associated with the corresponding increase

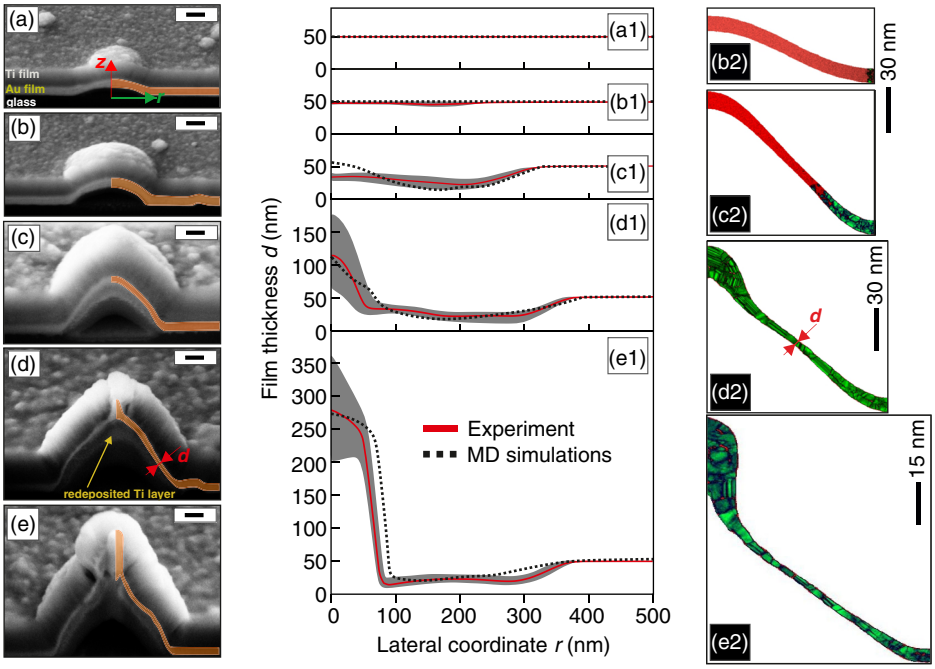

FIG. 2. (a)–(e) Side-view SEM images (view angle of 45°) of FIB cross-sectional cuts of single frozen-surface structures produced at the increasing absorbed fluence and previously shown in Figs. 1(a)–1(e), respectively. Orange areas in each image highlight the Au film and membrane. The scale bars for these images correspond to 100 nm. The darker gray layer under the Au layer, appearing in the images (c)–(e), is attributed to the redeposition of the Ti layer during the FIB milling, which is confirmed by the corresponding EDX measurements; (a1)–(e1) Film-membrane thickness d experimentally measured over 10 similar cuts of the 10 similar surface structures produced at the same irradiation conditions (red curves), and recalculated via corresponding MD simulations (black dotted curve) as a function of the lateral r-coordinate (cylindrical radius) defined in Fig. 2(a). Film-membrane thickness d is measured and recalculated in the directions normal to its local section [details are given in the inset in Fig. 3(b) below]. Gray areas indicate the error bar; (b2)–(e2) molecular-dynamics (MD) simulations showing the modification of the metal shell with absorbed energy. Red and green colors divide the molten and solid states of the film.

of the nanobump height. The subsequent evolution of the nanobump shape—from parabolic to conical—occurs at the further increase of the fluence [Figs. 2(d) and (d1)] accompanied by the accumulation of the molten material at the nanobump tip in the form of the 120-nm-high and 100-nm-wide protrusion. The lateral and vertical dimensions of this protrusion continuously increase versus the F value [Figs. 2(d), 2(e), 2(d1), and 2(e1)], forming a nanojet, while the surrounding nanobump becomes thinner through the jet-directed nanoscale hydrodynamic flow with its minimal experimentally observed thickness, reaching ≈13 nm near the nanojet edge and ≈20 nm near the nanobump edge. A further increase of the absorbed fluence stimulates the growth of the central protrusion [see Fig. 1(f) as well as Note 1 in the Appendix], while the surrounding shell continuously thins until its destruction accompanied by the formation of a micrometer-wide through hole [Fig. 1(g)].

Despite its straightforward character, such FIB cutting of surface nanotextures produced on noble-metal films, which are typically weakly resistant to electron- and ion-beam exposures, requires additional sample overcoating by some protective layer, mostly excluding its following practical nanophotonic applications. In this respect, nondestructive and noninvasive experimental methods, enabling a quantitative characterization of the supported nanoscale structures, are required. In this study, we have performed a nanoscale cross-sectional SEM-based EDX analysis schematically illustrated in Fig. 3(a) of the typical structures shown in Fig. 2(e). In this case, the EDX signal profile in the membrane normalized to that of the unperturbed film to give the corresponding membrane thickness profile. The advantage of the EDX acquisition is its almost nonperturbative character, as compared to the above-mentioned FIB-SEM combination. Indeed, FIB-SEM requires (i) deposition of a highly cohesive material (Ti) layer with the simultaneous release of very high cohesive energy (sublimation enthalpy of a few eV/atom), which can perturb—melt or even vaporize—the initial structure, if the Ti deposition rate and conduction of the releasing heat is inappropriately adjusted and, also, (ii) FIB cutting of the layered set can perturb the initial nanofeatures, if ion currents or the thickness of the deposited Ti layer are improperly chosen. Among these EDX-characterized surface nanostructures, the microbump, containing the small nanojet atop, provides the maximal metal thickness redistribution—from the 13-nm-thick cap of the bump to a few hundred-nm high protrusion—as it was previously confirmed by SEM

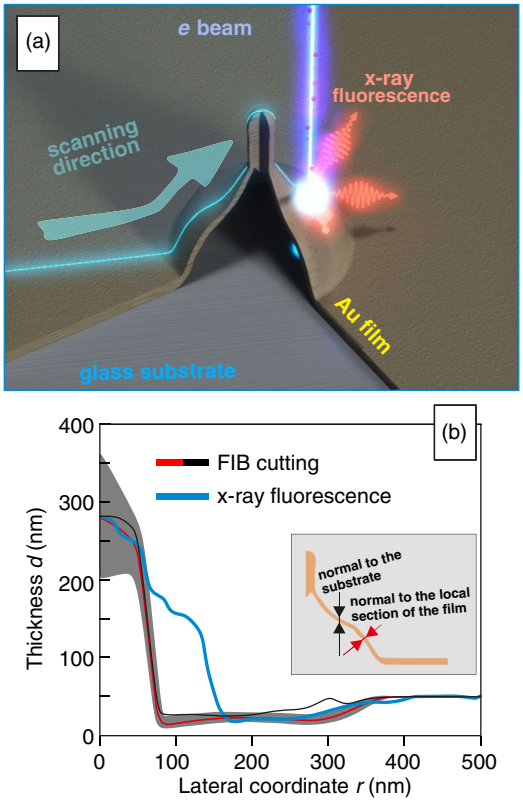

FIG. 3. (a) Sketch explaining the principle of the EDX profiling across the nanofeature by the *e*-beam excitation and subsequent detection of the characteristic x-ray fluorescence signal. (b) Radial profiles of film-membrane thickness measured using EDX cross-sectional analysis (blue curve) and FIB cutting–SEM visualization recalculated to present the film thickness in the direction normal to the substrate (black curve) and normal to the local section of the film-membrane (red curve). The inset shows the difference between the actual thickness along the normal to its local section and the top-view EDX-acquired thickness.

analysis of the FIB cuts. Additionally, the steep wall of the central protrusion in Fig. 2(e) represents almost a perfect object to estimate the lateral resolution of this SEM-based EDX approach.

EDX cross-sectional (radial) elemental microanalysis is carried out with a field-emission SEM microscope JEOL 7001F using an INCA Energy 350XT spectrometer (Oxford Instruments Analytical), at the electron energies of 10 and 30 keV, while the electron beam current is chosen at the level of 79 pA to avoid thermal damage of the nanostructures on the film. The acquisition of the EDX profiles for the laser-induced surface nanofeatures at the particular electron energies, which provide the penetration depths in the film and the supporting substrate much larger than the 50-nm film thickness, enables their calibration in terms of thickness, using the reference EDX-signal value for the nonirradiated gold film.

More specifically, the 30-keV electron beam provides too low and noisy EDX signals from the flattened regions of the thin Au film due to its very deep (2–3 μm) penetration through the film into the supporting substrate, but the 30-keV beam produces the appropriate EDX signals across the micron-tall nanofeatures, formed by the laser-driven melt accumulation (the central protrusion atop the nanobump). In contrast, the 10-keV electron beam provides reasonable EDX signals from the gold film and laser-induced features of comparable thickness, but is almost completely absorbed by the micron-tall surface features, excluding calibration of the corresponding EDX signals. As a result, the acquired cross-sectional EDX profiles are linked in the transition region from the thinned film within the bump and the tall central protrusion, representing the initial stage of the nanojet formation, with the 30-keV EDX signal in the center and 10-keV EDX signal at the periphery.

Figure 3(b) shows the EDX-profiling results for the thickness of the nanojet with the surrounding nanobump [Figs. 2(e) and 2(e1)] in comparison to the side-view SEM measurements of its thickness along the normal to the substrate, using the cross-sectional cuts. Both curves indicate a good agreement within the experimental error bars for all three topographies—the nonirradiated film, nanobump, and nanojet, supporting the relevance of both of these approaches. A minor difference in the spatial resolution of these approaches indicated by the 100-nm difference of the nanojet radius in Fig. 3, is a broadening artifact of an external electromagnetic noise in the local circuits during the prolongated EDX-profiling procedure of 3–5 min.

III. SIMULATION TECHNIQUE

In this study, a comprehensive simulation approach, including the two-temperature electron-ion hydrodynamics (2T-HD) and the classical molecular-dynamics method combined with Monte Carlo heat transfer by electrons (MD-MC) [46] is used, to represent the next step toward the accurate prediction of the translative flow-assisted redistribution of material after the ultrashort laser exposure. To achieve this goal, all relevant physical processes underlying the material response to such tightly localized ultrafast energy deposition in a skin layer should be taken into account. However, the simultaneous consideration of those multiple processes on the micrometer-sized scale during several nanoseconds with our simulation technique, including billions of interacting atoms and electrons, far exceeds the limits of available supercomputers; the largest and longest MD simulations [29,47,48] of laser ablation today operate with fewer 0.1×10^9 atoms and up to 3 ns only. To overcome this limitation, we divide all physical processes into "fast" and "slow" processes, and apply the 2T-HD or MD-MC model, respectively.

The 2T-HD model, describing the first short evolution stage with its typical duration of the order of acoustic time scale ($\approx$17 ps for our 50-nm-thick Au film and longitudinal speed of sound in gold of 3 km/s), includes one-dimensional 2T hydrodynamic code having a full 2T

physics: absorption laser energy, 2T electron thermal conduction, energy exchange between electrons and atomic vibrations via their coupling, and a 2T equation of state. Thus, the model takes into account all fast processes associated with electron pressure, electron conductivity, electron-ion temperature relaxation in gold lasting 7–10 ps [49], and separation of the molten film from the substrate with separation velocity $\nu_{\mathrm{c.m.}}(r)$ depending on the local stress $p(r)$ generated by isochoric laser heating of film up to lattice temperatures of a few thousand degrees produced by the absorbed fluence $F_{\mathrm{abs}}(r)$. 2T-HD calculations show that in 1–2 ps the electron heat conduction approximately homogeneously redistributes electron temperature T_e along the thickness of a film. After that normal to film gradient of T_e drops down but the 2T stage continues during 7–10 ps equilibrating electron and ion temperatures along the thickness. Thus, the temperature becomes dependent only on the lateral directions after the conclusion of the 2T stage. Fast homogenization of temperature takes place because the thickness of our gold film is less than the thickness of a heat-affected zone in a bulk gold [50,51].

The stress of $p(r) \sim 10$ GPa generated within the first stage, is responsible for the separation of film from the substrate. The 2T-HD model provides the separation velocities $\nu_{\mathrm{c.m.}} \approx (Z_s/Z_f)(p/B)c_s$ ranging from 0 to ≈60 m/s, where c_s is the longitudinal speed of sound in gold, B is the bulk modulus of gold, Z_s, Z_f are acoustic impedances of the substrate and the film, respectively, see details in Note 2 of the Appendix where a comparison between velocities $\nu_{\mathrm{c.m.}}$ in simulations and experiments is discussed.

The second, slow evolution stage starts after the separation of a film from the substrate and completes after the recrystallization of the molten cupola, which requires tens of nanoseconds typically. To simulate the slow processes initiated within the fast stage, the combined MD-MC approach is utilized. We (i) use known values for surface tension, density, and the coefficient of thermal conductivity together with (ii) the experimental lateral size of the cupola, thickness of a film, and the incident fluence in the tip, convert the incident fluence into absorbed fluence using a known value for the dielectric constant at our laser wavelength. Then, (iii) we use velocities from the hydrodynamic 2T-HD code for the particular experimental absorbed fluences. With all this, we calculate experimental dimensionless capillary and thermal parameters, shown below in this section and in the Appendix. Afterwards, we run the MD-MC code for these particular values of the two dimensionless parameters.

Then, the embedded atom method interatomic potential for gold is used [52], reproducing well the stress-strain and thermal characteristics of gold. The potential gives the density of melt about 16.9 g/cm^3 and the melting point of about 1330 K, which is close to the experimental $T_m = 1337$ K. The calculated surface tension of 0.546 J/m^2 is notably lower than the experimental $\sigma =$ 1.125 J/cm^2 at the melting temperature, see the discussion in the Appendix of Ref. [23].

The simulation parameters of two selected MD-MC calculations are presented in Table I. A thin film with a thickness d is placed in a square simulation box with dimensions $L_x = L_y = 140$ nm for the case "e" or $L_x = L_y = 270$ nm for the case "d". The periodical boundary conditions are imposed along the x and y axes. Then, the film is thermalized with the given radial temperature profile $T(r)$ with the fixed $T(r_c) = 1500$ K. After melting and equilibration the film gains the vertical-separation velocity $\nu_{\mathrm{c.m.}}(r) \sim \cos(\pi r/2r_c)$ with the maximum at the center, presented in Table I, and zero velocity at the r_c. Because the maximal temperature of the film is much less than the boiling temperature (≈3.2 kK), the saturated vapor pressure is too small to cause any dynamic effect on the moving film. Indeed, evaporation is not even observed in our MD simulations in the given temperature range.

MD-MC simulations reveal the translative flow-assisted redistribution of the molten film with MC heat transfer resulting in the subsequent resolidification of liquid via heat-conduction cooling of the hot cupolalike shell. The thermal diffusivity shown in Table I is adjusted by the MC electron jumping rate between neighbor atoms as described in Ref. [46]. A heat sink is simulated by using the Langevin thermostat with the typical temperature of 500 K for all atoms with $r > r_c$, which leads to the resolidification of film from its edge with time. This thermostat maintains also the zero-mass velocity outside the circle r_c, which keeps mechanically the film outside the circle at the substrate. This condition corresponds to the fixed boundary conditions implied at the edge r_c of the cupola.

The MD-MC simulation of a realistic micrometer-sized film having a very large amount of involved atoms (∼10^9) during a long cooling time of many tens of nanoseconds is

TABLE I. Parameters of MD-MC simulations for two regimes of mass redistribution leading to the formation of either bumps or jets. This makes it possible to plot the theoretical boundary between these regimes marked as points "d" and "e" in Fig. 4. The corresponding final structures obtained in the simulation are shown in Figs. 2(d1), 2(d2), 2(e1), and 2(e2).

No.	N_{atoms}	$2r_c$ (nm)	d (nm)	χ (cm^2/s)	ν_{cm} (m/s)	ν_σ (m/s)	ν_χ (m/s)	V_σ	V_κ
d	44×10^6	260	10	0.18	200	106	69	0.529	0.346
e	6×10^6	130	5.1	0.18	385	148	138	0.384	0.358

not feasible on the available computers. Instead, the small-sized films with several millions of atoms are simulated (Table I). To meet the experimental conditions, the scaling approach [30] is used. Two nondimensional parameters, governing the evolution of film separating from the substrate with the velocity $\nu_{\mathrm{c.m.}}$, are the capillary parameter

$$V_\sigma = \nu_\sigma/\nu_{\mathrm{c.m.}} \tag{1}$$

and the thermal parameter

$$V_\kappa = \nu_\chi/\nu_{\mathrm{c.m.}}, \tag{2}$$

where the capillary velocity ν_σ and the thermal velocity ν_χ are defined as

$$\nu_\sigma = 2\sqrt{\sigma/(\rho d)}, \qquad \nu_\chi = \chi/(2r_c). \tag{3}$$

Here, χ is the thermal diffusivity, σ the surface tension, ρ the initial density, d the initial thickness of metal film, and r_c the separation radius. These governing parameters are also listed in Table I.

IV. REGIMES OF MASS REDISTRIBUTION FROM EXPERIMENTS AND SIMULATIONS

Analysis of the FIB cuts performed on surface features produced at the different incident pulse energies [Figs. 2(a)–2(e)] indicates several steps, characterizing the molten film evolution via corresponding translative hydrodynamic flows and affecting the resulting thickness distribution along the produced surface structure: (i) inflation of the metal film in the form of the parabolic-shaped cupola, having a constant thickness along its circumference; (ii) weak redistribution of the cupola thickness; (iii) transformation from parabolic to conical shape; and, finally, (iv) appearance of the central protrusion.

Despite the downscaled computation dimensions used in MD-MC simulations, all these steps are perfectly reproduced in our theoretical model by varying the thermal and capillary parameters [Figs. 2(b)–2(e2)], which both depend on the absorbed fluence F, in their turn. Here, to illustrate the film thickness distribution for parabola-shaped bumps [Figs. 2(b2) and 2(c2)] a few simulated snapshots are taken at different times, when the moving metal film is not completely frozen (red and green colors divide the molten and resolidified states of the film). By increasing the heat conductivity in the MD-MC simulations, the completely resolidified parabola-shaped bumps with the negligible redistribution of mass along the film can be obtained. In the case when redistribution of mass is weak the final thickness is approximately equal to the initial thickness. This conclusion is in agreement with our previous two-dimensional (2D) MD-MC simulations showing the weakening of the redistribution when absorbed energy is small and conduction cooling is fast [23,53]. The frozen shapes are similar for 2D and three-dimensional (3D) geometries in case of fast cooling. Upscaling the film thickness via thin-shell recalculation [53] also gives a perfect qualitative agreement with the experimentally measured thickness distributions for all surface structures [Figs. 2(a1)–2(e1)], providing the reliable way for a theoretical simulation of the fabricated surface 3D features.

Other common surface structures, such as high-aspect-ratio nanojets and through holes [Figs. 1(f)–1(h)], can be also reproduced by varying the capillary and thermal parameters in the MD-MC simulation. Carrying out such simulations as well as using our recently published results [30], we have built the map of the corresponding nondimensional governing parameters required to reproduce the certain type of the structure, where the transitions (or boundaries) between "bump-jet" and "jet-hole" regimes are marked with the transition blue-green and green-red strips, respectively (see Fig. 4). Specifically, two important dots marked as "*d*" and "*e*" letters, reflecting the parameter set for MD-MC simulations from Figs. 2(d2) and 2(e2) as well as establishing the theoretical bump-jet regime boundary, are indicated in this map. These two important regimes can be formally divided according to relative translative-flow assisted mass redistribution of the molten film near the bump tip. This separation follows from the analysis of the simulated structures with moderate and significant material redistribution near the structure central axis [Figs. 2(d2) and 2(e2), respectively]. A similar formal separation can also be applied for our experimental results [see Figs. 1(d), 1(e), and 1(h), and discussions below]. The corresponding parameter set for *d* and *e* dots are summarized in the Table I.

We estimate the thermal and capillary parameters, which correspond to our five main experimental points [see Figs. 2(a1)–2(e1)] on the (V_σ, V_κ) parameter plane (hollow circles in Fig. 4) using the typical diameter of the bump $2r_c \approx 900$ nm from Fig. 1(h) and corresponding Eqs. (1)–(3). Taking into account the temperature-dependent surface tension of molten gold ≈ 0.9 J/m^2 [23] and the thermal diffusivity $\chi \approx 0.5$ cm^2/s, for our 50-nm-thick Au film the thermal and capillary velocities are equal to $\nu_\chi \approx 56$ m/s and $\nu_\sigma \approx 61$ m/s, respectively. Although the experimental values of σ, κ, r_c, and the corresponding velocities ν_σ and ν_κ are well defined, the experimental separation velocity $\nu_{\mathrm{c.m.}}$, required to estimate the V_σ and V_κ, is an unknown parameter.

For the fixed diameter of the optical spot and the absorption coefficient A weakly dependent on the incident fluence F_{inc}, which holds true in our energy range, the absorbed fluence F_{abs} will be proportional to the pulse energy E. On the other hand, according to our 2T-HD simulations of the separation stage and considering negligibly weak adhesion between the Au film and the silica substrate, the velocity $\nu_{\mathrm{c.m.}}$ is proportional to the applied pulse energy E [53]. Using this proportion and assuming that

$$\nu_{\mathrm{c.m.}}(E) = (\nu_{\mathrm{c.m.}}|_{E=1.7})(E/1.7), \quad (4)$$

where E is given in nJ and $\nu_{\mathrm{c.m.}}|_{E=1.7}$ is an adjustable separation velocity at $E = 1.7$ nJ (the corresponding absorbed fluence is 47.8 mJ/cm^2), one can obtain the set of the governing parameters on the capillary-thermal plane (V_σ, V_κ) (1), (2) related to our particular experimental cases for the fixed $\nu_{\mathrm{c.m.}}|_{E=1.7}$ value.

To obtain the separation velocity $\nu_{\mathrm{c.m.}}$ as a function of the absorbed fluence F_{abs} and assess its reliable value, the one-dimensional 2T-HD modeling of film on the glass substrate is performed (see Note 2 in the Appendix for details). Assuming the $\nu_{\mathrm{c.m.}}|E = 1.7 = 110$ m/s and using Eq. (4), we obtain the set of governing parameters on the (V_σ, V_κ) plane (hollow markers in Fig. 4), which corresponds to our experimental results [Figs. 2(a1)–2(e1)]. An analysis of the parameter plane indicates that the experimental bump-jet transition boundary (dashed curve in Fig. 4) defined by the surface structures obtained at absorbed fluences 45.2 and 47.8 mJ/cm^2 (blue and green hollow circles, respectively) is located ~30%–40% higher than the corresponding boundary estimated from the analysis of the simulation results. This deviation can be explained by the difference in conditions. The boundary condition established in our MD-MC simulations poorly reproduces a real experimental situation since the heat sink and the area defining the mechanical attachment of a bump to the substrate are much closer to the edge of the simulated bump (see Appendix). Under such circumstances, the simulated shell is stronger, thus shifting the theoretical transition boundary closer to the point of origin in Fig. 4.

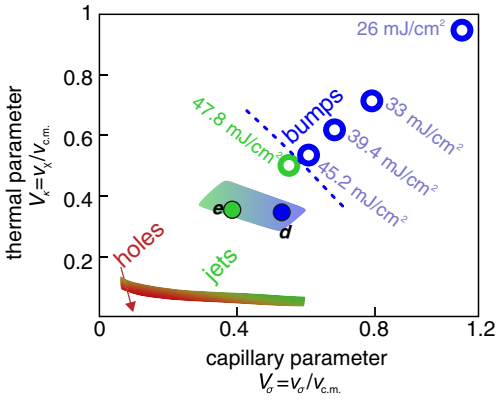

FIG. 4. The map of the thermal V_σ and capillary V_κ parameters. The filled markers "*d*" and "*e*" indicate the simulated parameters used to obtain the resolidified geometries presented in Figs. 2(d2) and 2(e2), respectively. Other simulated markers used to accumulate statistics on the corresponding regimes are not shown to avoid overburdening of the figure. Instead, two gradient-color stripes are used to show the characteristic "hole-jet" (red-green) and "jet-bump" (green-blue) transition boundaries provided by the MD-MC simulations. The experimental capillary and thermal parameters marked as hollow markers are estimated considering the separation velocity of $\nu_{\mathrm{c.m.}} = 110$ m/s at absorbed fluence of 47.8 mJ/cm^2 (see text for details). The corresponding absorbed fluence (in mJ/cm^2) is indicated near each hollow marker. The dashed line shows the experimental jet-bump regime boundary. The colors of the markers (both filled and hollow) indicate the transition between different fluence-dependent regimes providing formation of the bumps (blue) and the jets (green), while the similar color scheme is used to divide the corresponding pulse energy–fluence ranges in Fig. 1(h).

Finally, it is plausible that the relative ratio between the bump-jet and jet-hole threshold boundaries is weakly sensitive to the difference in the mentioned boundary conditions. The experimentally measured ratio of the characteristic threshold energies required for the formation of the through hole and the jet [corresponding energy logarithms $\ln(E)$ are equal to 1.9 and 0.65 in Fig. 1(h)] is about 3.5. Analysis of the calculated capillary-thermal parameter map (position of the gradient-color stripes in Fig. 4) gives the ratio equal to 3.6. This ratio is calculated measuring the distances from the origin of the two characteristic dots on the intersection of the diagonal line in Fig. 4 and the theoretical bump-jet and jet-hole threshold boundaries. Thus, the theoretical and experimental results are in satisfactorily good agreement with each other.

V. CONCLUSIONS AND OUTLOOK

Experimental procedures based on the SEM inspection of nanoscale focused ion beam cross sections and energy-dispersive x-ray fluorescence nanoscale profiling, demonstrate a consistent nanoscale invasive and noninvasive characterization of mass-density distributions within individual radially symmetric topological surface structures—separate nanobumps and jets on nanobumps, produced by a single-shot ablation of 50-nm-thick glass-supported gold films by tightly focused fs-laser pulses at variable pulse energies. More specifically, radial mass distribution (thickness) across the individual features is quantitatively acquired either by their nanoscale focused-ion beam cutting and following side-view electron microscopy analysis, or by direct top-view radial nanoprofiling of their relative thickness using energy-dispersive x-ray fluorescence spectroscopy at different electron-beam energies, calibrated by the signal from the unperturbed film. These demonstrated advanced characterization approaches pave the way to detailed modeling of a near-field electromagnetic response of fabricated metasurfaces and can be adopted for fully automated noninvasive in-line control during high-throughput large-scale laser fabrication.

Comparative molecular-dynamics simulations are undertaken to envision spatiotemporal dynamics of the underlying nanoscale hydrodynamic melt flows and are shown to provide quantitative predictions of the evolution of the metal film thickness, enabling in the future realistic predictions of more-complex 3D nanostructures and 3D-structured nanomaterials [54] produced by focused ultrashort laser pulses, carrying, for example, angular

momentum [55–59] (vortex laser pulses), and accurate simulations of more-complicated systems, such as materials with new metastable amorphous and crystalline phases [60,61], phase-change materials [62,63], or metallic glasses [64]. In this line, the quantitative characterization of the mass distribution profiles for the laser-fabricated 3D nanoscale structures lays down a solid basis for solution of the reverse problem, related to evolution dynamics on nanostructures to benchmark theoretical models.

ACKNOWLEDGMENTS

The main experimental part of this research is supported by the Russian Science Foundation (Grant No. 17-19-01325). S. J. acknowledges the Workshop of Photonics R&D. Ltd. for the laser fabrication setup acquired via a collaborative grant and the Australian Research Council DP170100131 Discovery project. In the part of EDX characterization, S. I. K. is grateful for the financial support by the Government of the Russian Federation (Grant No. 074-U01) through the ITMO Visiting Professorship Program. V. V. Z. and N. A. I. are responsible for the theoretical part of the paper, simulations, and comparison with experimental data; they acknowledge the grant of the Russian Science Foundation (Project No. 14-19-01599).

APPENDIX: ADDITIONAL INFORMATION

Note 1. Pronounced jet atop the nanobump.—Figure 5 shows the tilted SEM image of a high-aspect-ratio nanojet produced at absorbed fluence of 56.8 $\mathrm{mJ/cm^2}$. This snapshot illustrates the formation of the 900-nm-high jet above the cupola as well as the starting point of the formation process of the spherical-shape droplet, which will be ejected at increased absorbed fluence. The modulation of the thickness along the nanojet height manifests development of the Rayleigh-Plateau hydrodynamic instability acting on the molten metal moving upward along the jet.

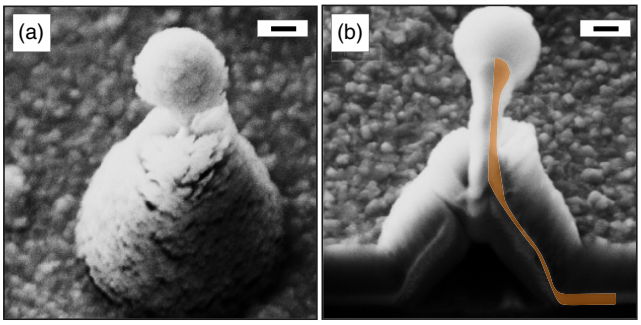

FIG. 5. Side-view SEM images (view angle of 45°) of the nanojet produced at absorbed fluence of 57 $\mathrm{mJ/cm^2}$ (a) and its FIB cross-sectional central cut (b). The nanojet is overcoated with a 200-nm-thick protective Ti layer. The first SEM image (a) illustrates the nonuniform coverage with the Ti overlayer. Orange areas in the second image (b) highlight the Au film-membrane. The scale bars for both images correspond to 100 nm.

Note 2. Internal rupture.—Because the experimental separation velocity is adjusted to provide the agreement between experimental and simulation results, additional discussion is given here to substantiate the chosen separation velocity

$$\nu_{\mathrm{c.m.}}|_{E=1.7} = 110\ \mathrm{m/s}.$$

To estimate the dependence of the $\nu_{\mathrm{c.m.}}$ on the absorbed fluence F_{abs}, we have carried out the one-dimensional 2T-HD simulations neglecting the adhesion of gold to the silica substrate thanks to the hydrophobic property of silica against molten gold. The 2T-HD simulations show that the film is homogeneously heated across its thickness d during ≈1 ps after the ultrashort pulse irradiation [53]. Fast spreading of absorbed energy from a skin layer proceeds due to an electron thermal conductivity strongly enhanced at the 2T stage. According to our simulations [see Fig. 6(a)], below the threshold F_{rup} of the internal rupture of a film, a film separates as a whole from substrate at the velocity $\nu_{\mathrm{c.m.}}(F_{\mathrm{abs}})$. This accumulation continues during the temporal interval when a film remains in mechanical contact with the substrate. Velocity $\nu_{\mathrm{c.m.}}(F_{\mathrm{abs}})$ is obtained *after* the instant of separation by averaging local velocities over the film thickness. Thus, velocity $\nu_{\mathrm{c.m.}}$. represent a velocity of a center of mass (c.m.) of a film.

Two rarefaction waves V and C running towards each other from the "vacuum-film" (V, vacuum) and "substrate-film" (C, contact) boundaries create a layer with a negative pressure p_{tensl} near the middle plane of a film; see details in Refs. [23,53]. These two waves begin to interact at an acoustic time scale $t \approx t_s/2$; $t_s = d/c_s$, d is the thickness of a film, c_s is a sound speed. For fluences $F < F_{\mathrm{rup}}$ the tensile stress $|p_{\mathrm{tensl}}|$ created by V-C interaction is below the material strength p_{strength} of gold. Thus, at such conditions the film survives under stretching (no internal rupture).

If the film survives, then the wave V running from the vacuum side continues its run in the direction to the contact (the boundary between a film and substrate). The wave V arrives at the contact at the instant $t \approx t_s$. Pressure $p_c(t)$ at the contact evolves over time. The acoustic impedance of gold Z_g is approximately 7 times larger than the impedance of silica Z_s. Pressure p_c is significantly less than the pressures p in the bulk of a film: $p_c \approx (Z_s/Z_g)p$. When the wave V achieves the contact then the function $p_c(t)$ changes its sign from positive to negative [23,53]. Adhesion is small, therefore, the separation of a film as a whole from substrate [shown in the upper picture in the left column in Fig. 6(b)] begins around the time $t \approx t_s$. The separation is caused by the tensile action of the wave V onto the contact.

The situation changes dramatically if $F > F_{\mathrm{rup}}$, the tensile stress $|p_{\mathrm{tensl}}|$ overcomes the strength p_{strength}, and the film begins to split into the vacuum and the contact parts *before* the rupture of the contact. This is shown in the

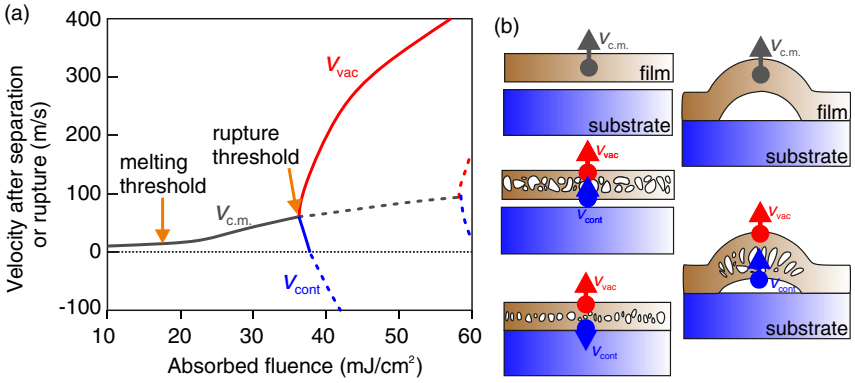

FIG. 6. (a) Velocity $\nu_{\text{c.m.}}$ of the separated metal film as a function of the absorbed fluence F_{abs}. There are two different fluence-dependent separation regimes schematically shown in the left column of (b). At the fluences F_{abs} lower than the rupture threshold F_{rup} the film separates as a whole having the local center-of-mass velocity $\nu_{\text{c.m.}}(F_{\text{abs}})$ [see the upper picture in the left column in (b)], while at higher fluences the film splits into "vacuum" and "contact" parts having averaged velocities $\nu_{\text{vac}}(F_{\text{abs}})$ and $\nu_{\text{cont}}(F_{\text{abs}})$, respectively; see the middle and bottom diagrams in the left column in (b).

middle and bottom diagrams in the left column in Fig. 6(b). Velocities ν_{vac} and ν_{cont} in these two diagrams refer to the vacuum and the contact parts of a film at the stage when the parts lose their mechanical connections. Values ν_{vac} and ν_{cont} are obtained by averaging along thicknesses of the vacuum and the contact parts.

As is said, the ratio of impedances of gold Z_g to silica Z_s is large. Therefore, the expansion of a film after the action of an ultrashort laser pulse is approximately symmetric relative to the middle plane of a film. A small deviation from symmetry is caused by a small but finite ratio of impedances Z_s/Z_g (and also because $d < d_T$, but not $d \ll d_T$, where d_T is the thickness of a heat-affected zone). In the case when $Z_s/Z_g = 0$ and the film is thin (thus, it is almost homogeneously heated across its thickness), the velocity $\nu_{\text{c.m.}}$ is ≈ 0 in spite of significant expansion velocities. The expansion velocities connected with the rarefaction waves V and C are opposite in their directions and compensate each other giving a resulting small velocity of the center of mass $\nu_{\text{c.m.}}(F_{\text{abs}})$ if $F < F_{\text{rup}}$; see Fig. 6(a).

Above the rupture threshold F_{rup} the center-of-mass velocities ν_{vac} and ν_{cont} of the vacuum and the contact parts are split; for $F < F_{\text{rup}}$ we can formally write $\nu_{\text{c.m.}} = \nu_{\text{vac}} + \nu_{\text{cont}}$. There is a short interval near the F_{rup} in Fig. 6(a) where velocities ν_{vac} and ν_{cont} have the same sign directed into the vacuum side. The situation corresponding to this interval is illustrated by the middle scheme in the left column of Fig. 6(b).

Above this interval the contact part moves in the direction of the substrate. The continuation of the $\nu_{\text{cont}}(F_{\text{abs}})$ into the range of negative velocities $\nu_{\text{cont}} < 0$ is shown by the bottom dashed curve in Fig. 6(a). Of course, this is the conventional curve because the magnitudes $\nu_{\text{cont}}(F_{\text{abs}}) < 0$ are not asymptotic magnitudes $t \to \infty$ conserved in time. (Here, we consider the 1D case when deceleration action of the surface tension is absent. This action becomes significant in the case of a finite-size irradiation spot). 2T-HD simulations and analytic analysis show that dense gold (with high Z_g) from the contact part presses the less dense silica (with low Z_s) supporting positive contact pressure $p_c(t)$ exponentially decaying in time $p_c(t) \propto \exp(-t/t_{\text{decay}})$ with e-folding time t_{decay} of the order of t_s. This pressure decelerates the motion of the contact part and thus decreases velocity $\nu_{\text{cont}}(t)$.

We are sure that at the acoustic time scale $\sim t_s$ the velocity of the contact part remains directed to the substrate side (no separation from substrate). The fate of the contact part of the gold film at the late stage $t \gg t_s$ is unclear. At least in our experiments with an extremely small irradiation spot $r_c = 300$–400 nm described in this paper [see Figs. 2(a1)–2(e1)] we don't see remnants of gold on the surface of silica inside the cavity under the shell of the bump. Maybe the liquid gold film fragments into a set of droplets on a surface of hydrophobic silica, and the droplets move to the periphery of the circle under the shell under the action of 3D effects and velocities directed along the surface; also partial evaporation and redeposition onto the rear side of the shell takes place.

Near the threshold $F > F_{\text{rup}}$ the velocity ν_{vac} quickly increases with the difference $F - F_{\text{rup}} > 0$, see Fig. 6(a). Below the threshold $F < F_{\text{rup}}$ the momentum

$$I = \int_{-\infty}^{ts/2} p(x = d/2, t)dt \qquad \text{(A1)}$$

moving the vacuum part of a film is compensated by the resistance of condensed gold to stretching, here $p(x = d/2, t)$ is pressure in the middle of the film. If we overcome the threshold F_{rup} to a few tens of percents, then the countermomentum produced by the resistance force of condensed matter becomes small relative to the momentum (A1). Then the center-of-mass velocity of the vacuum part is $\nu_{\text{vac}} \approx I/(\rho d/2)$. This velocity roughly is $Z_g/Z_s \approx 7$ times larger than velocity $\nu_{\text{c.m.}}$ near threshold. This explains the growth of $\nu_{\text{vac}}(F_{\text{abs}})$ above threshold F_{rup} in Fig. 6(a).

According to the particular series of the 1D 2T-HD simulations summarized in Fig. 6(a), the values $F_{\text{abs}}|_{\text{rup}}$, $\nu_{\text{c.m.}}|_{\text{rup}}$ describing the threshold of rupture are rather small: $F_{\text{abs}}|_{\text{rup}} \approx 40$ mJ/cm^2, $\nu_{\text{c.m.}}|_{\text{rup}} \approx 60$ m/s. The large ratio Z_g/Z_s results in a decreasing velocity $\nu_{\text{c.m.}}$ and an increasing susceptibility of velocity $\nu_{\text{vac}}(F_{\text{abs}})$ to the raising of

energy F_{abs} above the threshold F_{rup}, see Fig. 6(a). Why do we say that the values $F_{abs}|_{rup}$ and $\nu_{c.m.}|_{rup}$ are small? Explanations are given below. The main problem is connected with the comparison of relative positions of the rupture threshold F_{rup} from Fig. 6 and the threshold F_{hole} from Fig. 4 for the appearance of a through hole; we compare their positions on the energy axis in Fig. 6. Figure 6 presents the fast stage, it doesn't know about capillary forces r_c, and the rate of slow cooling at the one-temperature stage. Definitely, $F_{hole} < F_{rup}$ for large spots r_c; indeed, for r_c equal to many tens of microns, the capillarity can stop the separated shell only very far away, at distances $\sim r_c$; but it seems that the shell will break off before the stopping; cooling is too slow for large r_c to freeze the shell; only edges are frozen. But for small spots the situation is different, as we will see below.

Let $\nu_\sigma \approx \nu_\chi$ (3), then we are near the bisectrix of the angle between the horizontal and vertical axes in Fig. 4. The bisectrix cuts the bumps-jets and jets-holes boundaries taken from simulations at the points $V_\sigma = V_\kappa \approx 0.38$ and ≈ 0.1, respectively.

In our experiments, the boundary conditions are softer than in MD-MC simulation: only at the infinity a film is held on the substrate (adhesion is weak) and only at the infinity the temperature returns to the initial temperature of a film equal to 300 K. While in MD-MC simulation a film is held on the substrate in the narrow rim around the radius r_c; and cooling of the inflated shell is carried on by supporting the fixed temperature below the melting temperature in this rim, see Sec. III.

If we use the softer conditions in simulations, then the threshold velocity $\nu_{c.m.}$. necessary to shift from the regime with bumps to the regime with jets will be smaller, because the cupola is weaker mechanically connected to the film and the cooling rate is lower since the cold bath–sink is more distant. The estimates give a 30%–40% decrease of the threshold velocity $\nu_{c.m.}$. Thus, the intersections of the bisectrix with the bump-jet and jet-hole boundaries in conditions closer to the experiment will be in the points $V_\sigma = V_\kappa \sim 0.54$ and ~ 0.14, respectively.

In our experiments, $v_\sigma \approx 60$ m/s, $v_\chi \approx 60$ m/s (3), see Sec. IV. If we take the threshold values $V_\sigma = V_\kappa \sim 0.54$ and ~ 0.14 corrected above, then the bumps exist in the range of velocities $0 < \nu_{c.m.} < 110$ m/s, while the jets and holes appear when $110 < \nu_{c.m.} < 400$ m/s and $\nu_{c.m.} > 400$ m/s, respectively. Comparing these high velocities with those in Fig. 6(a), we see that the bumps, jets, and through holes fall into the set of cases above the rupture threshold.

The rupture threshold F_{rup} in Fig. 6(a) has been found from the 1D 2T-HD runs. The value F_{rup} depends on the model of nucleation used in the code. The model has been presented in Ref. [65]. The model is adjusted to the spallation results of MD-MC simulations [66] and may somewhat underestimate the material strength of gold. If we calculate energy density $\epsilon_{rup} = F_{rup}/d$ before the bulk expansion stage at the threshold $F_{rup} = 36$ mJ/cm^2 for $d = 60$ nm as in Fig. 6(a), then we will obtain $\epsilon_{rup} \approx 0.64$ eV/atom. The heat of vaporization (cohesive energy E_{coh}) of gold is 342 kJ/mol = 3.4 eV/atom. According to Ref. [67], the ablation threshold F_{abl} for a freestanding Al or Cu film is 28%–30% of E_{coh}; above the threshold F_{abl} the freestanding film separates into two halves; thus, the ablation threshold is equivalent to the rupture threshold above which a film also separates into two parts. Cu is similar to gold, therefore $\epsilon_{rup} =$ 0.95–1 eV/atom according to Ref. [67].

The shift from $\epsilon_{rup} \approx 0.64$ to 0.95–1 eV/atom increases F_{rup} and $\nu_{c.m.}|_{rup}$ to 60 mJ/cm^2 and 90 m/s. A corresponding continuation of the regime of separation as a whole with dependence $\nu_{c.m.}(F_{abs})$ and the shift of the threshold F_{rup} are shown in Fig. 6(a) by the dashed-line curve split at the end point to two branches. Additional corrections are related (i) to the small decrease of the threshold ϵ_{rup} from the value 0.95–1 eV/atom because film in our 1D 2T-HD simulations is 2–3 times thicker than the films studied in Ref. [67]; (ii) and with the small increase (from the value $0.95 - 1$ eV/atom) proportional to Z_s/Z_g since due to the presence of a substrate the rarefaction wave C coming to the middle of the film from the substrate side is weaker than the rarefaction produced by the expansion into vacuum (the substrate becomes mechanically equivalent to vacuum in the limit $Z_s/Z_g \to 0$).

Additional factors increasing the threshold F_{rup} in Fig. 6(a) are linked to (i) an increase of resistance to stretching thanks to the existence of foam and to (ii) the 3D character of blistering [see the diagrams on the right-hand side of Fig. 6(b)]. These factors are illustrated in Fig. 6(b). The middle and bottom diagrams in the left column in Fig. 6(b) schematically present membranes in the foam in the plane case: $r_c = \infty$. The membranes mechanically link the vacuum and contact parts of the film after nucleation. These links reinforce a film against rupture. For the same reasons, the nucleation threshold is lower than the ablation threshold [20,26]. This is why the frozen cavities remain. But comparisons made in Note 4 below don't give significant changes in the thresholds.

In the model of rupture, used in the 1D 2T-HD code, the condensed matter is ruptured (pressure drops to zero) as the criterium of nucleation is fulfilled. Of course, this is an approximation. The real situation is shown in Fig. 6(b). The foam and the curvature of the bump may hamper the total rupture, thus increasing the values F_{rup} and $\nu_{c.m.}|_{rup}$ against the values given by the 1D 2T-HD code. But the discussion in Note 4 does not support this suggestion.

The analysis presented above shows that even in the range of high fluences $F_{abs} = 40$–80 mJ/cm^2 it is still possible to keep the bump with the jet structures at the surface of the substrate (avoiding its total rupture and formation of a through hole) in spite of high values of

velocity ν_{vac}. This is possible due to the high NA of the lens yielding in the relatively small (relative to previous experiments) size of an irradiated spot $R_{opt} = 600$ nm, see Fig. 2.

Velocity ν_{vac} is established after the breaking of the mechanical connection through the foam between the vacuum and contact parts of the film. The only slow mechanical deceleration by surface tension directed tangentially along the surface of the vacuum part remains after the rupture of the foam. This kind of deceleration appears due to ties of the flying vacuum part with the solid film outside the separation radius. This deceleration becomes more significant with an increase of curvature of the flying film. Until the foam survives, the curvature is small and the deceleration of the vacuum part is accomplished by the liquid membranes forming the foam; this is illustrated in the left column in Fig. 6(b). At this stage the forces are directed normally to the surface of the vacuum part.

It should be mentioned again that below the rupture threshold F_{rup} the film separates as a whole. Thus, the rear side (opposite to the vacuum side) of the shell of the bump is smooth [see the upper diagrams in the left and right columns in Fig. 6(b)] because the contact between a film and substrate is smooth and the separation (the rupture of a contact) of a film from the substrate is continuous (no random nucleations). Above threshold F_{rup} the internal rupture of a film takes place. This process begins with random nucleations in the middle of the film [see the bottom diagrams in Fig. 6(b)]. The process continues with the formation of a two-phase liquid-vapor mixture transforming gradually into foam between the vacuum and contact parts of the film separated later from each other. This stage is shown in the bottom diagrams in Fig. 6(b), see also Note 4.

As it was mentioned above, the liquid membranes inside the foam connect mechanically and thermally the vacuum and contact parts during some time period. Because of mechanical connections, the vacuum part is slightly decelerated during this transition stage (transition from the connected stage to the separated stage). The thermal connections cool the vacuum part through foam. The remnants of the foam exist for some time at the rear side of the vacuum part. Thus, above the threshold F_{rup} for some time the rear side cannot be regarded as a smooth surface opposite to the cases below threshold F_{rup}; compare the top and bottom diagrams in the right column in Fig. 6(b); see also Fig. 7.

High values of velocity ν_{vac} mean that the first droplet will also have a high velocity. This droplet appears above the threshold for the separation of the first droplet from the jet. The first droplets fly perpendicularly to the surface of the substrate with a very narrow angular distribution. Thus, using a high-NA lens producing an extremely small optical spot provides the way to produce such fast, exactly directed droplets, a feature crucial for LIFT laser printing technology.

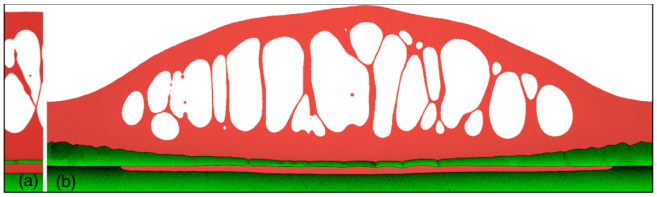

FIG. 7. Influence of curvature and nonlocal lateral interactions on dynamics. $t = 665$ ps. (a) 1D MD run (No. 353). 1D means that $r_c = \infty$ and average lateral gradients are equal to zero. Periodic boundary conditions are imposed on the lateral sides of the computational rectangle. (b) 3D MD run (No. 355), 192×10^6 atoms. Periodic boundary conditions are used on the lateral sides. The spatial period between the sides is 1000 nm. Both runs correspond to $F/F_{rup} = 1.4$, where F_{rup} is the rupture threshold; in 3D the value F is fluence in the tip. Initial structures of both runs along the normal direction are similar: there are the gold film 100-nm thick and underlying glass layer (substrate) 250–500-nm thick. Simulations show that lateral gradients defined by the aspect ratio 100:1000 of thickness to lateral period weakly influence the expansion; see also Fig. 8 and text. This conclusion follows from the comparison of heights of the vacuum boundaries. Colors present values of the symmetry parameter: red refers to liquid Au and glass, while green refers to solid Au and glass.

Note 3. Nonlinear absorption.—Absorption coefficient A depends on a state (electron and ion temperatures, density, transition layer) of reflecting matter and surface of a target. In reference books, e.g., Refs. [39,40], values A are measured under normal conditions and for clean surfaces. Coefficient A may strongly change even during an ultrashort (tens or hundreds of femtosecond) pulse, see, e.g., Ref. [68] where pump-probe measurements are employed and a strong enhancement of the absorption due to the thermal excitation of d-band electrons of gold is observed. This change influences the absorption of a pump pulse. The effect is very important in the case when prior to a pulse an absorption is weak $A \sim 1\%$. Changing reflection R from 99% to 70% will increase the absorption $\times$ 30.

Coefficient $A \sim 1\%$–10% relates to well-reflecting metals and photon energies ϵ outside their d bands; for gold $\epsilon < 2$ eV. Namely, in this case the nonlinear enhancement of absorption is important. For metals with a d band around the Fermi level (like Pt, Ta) or metals like gold illuminated by harder photons ($\epsilon > 2.2$ eV for Au) the effect of changing of absorption A is much less significant; see the comparison between Ag and Pt dependencies A ($\lambda = \text{fixed}, F_{inc}$) in Ref. [69], $\lambda = 800$ nm $=$ fixed in Ref. [69] is below the d-band edge for Ag. In all of these cases the absorption A is high (tens of percent) in the linear conditions (when the intensity of illumination is infinitesimally low). According to Ref. [69], in cases with highly reflecting metals, appreciable changes in the absorption of a pump pulse begin when the absorbed fluence is higher than $\sim$20 mJ/cm^2. Value $A \approx 0.35$ for our $\epsilon =$ 2.41 eV on gold does not change during pulse in our range of fluences.

Note 4. Discussion.—Note 2 above is devoted to physical reasons why the rupture threshold appears. The reasons are the same as in the case of free-standing film previously considered [66,67]. 2T-HD gives the threshold value $F_{\rm rup} = 36$ mJ/cm^2 for 60-nm film, see Fig. 4. The situation with film and substrate has been considered in Ref. [70] by MD methods. There is a 100-nm Au film strongly attached to the glass substrate (large cohesion). Thus, as the absorbed fluence increases, only internal rupture is possible. Value $F_{\rm rup} = 46.5$ mJ/cm^2 in Ref. [70]. This value is rather close to $F_{\rm rup} = 36$ mJ/cm^2 if we use proportion to mass $46.5 \times 60/100 = 28$ mJ/cm^2; mass is proportional to thickness. The increase of contact cohesion shifts the separation threshold to the upper values. Separation disappears when the separation threshold overcomes the threshold $F_{\rm rup}$. The value $F_{\rm rup}$ doesn't depend on cohesion, because rupture takes place before the stretching of contact begins (see Note 2).

Comparisons between 1D 2T-HD, 1D MD, and 3D MD are shown in Figs. 7–9. Figures 7 and 8 present 1D and 3D-2D MD runs (brief information about these simulations is given in Ref. [70]). They are compared in order to understand the importance of lateral gradients. In 1D MD an irradiated spot is infinitely large $r_c = \infty$ and the average lateral gradients are equal to zero. The 3D-2D MD run corresponds to the spot with finite lateral size $r_c \approx 1000/2 = 500$ nm. Mass distributions $\langle\rho(x)\rangle$ in Fig. 8 are obtained by averaging

$$\langle\rho(x,t)\rangle = (L_y L_z)^{-1} \int_y \int_z \rho(x,y,z,t)\,dy\,dz, \qquad \text{(A2)}$$

where L_y, L_z are dimensions of the rectangular cross section $x = \text{const}$ of the simulation box, $\int_y \int_z$ means the integration over this cross section. In 3D-2D geometry the plane $x = \text{const}$ crosses mass curved due to finite size r_c of the illumination spot. Therefore, 3D-2D distribution $\langle\rho\rangle$ in Fig. 8 is more smeared along the x axis relative to the 1D distribution. Comparing 1D and 3D-2D we conclude that the influence of finite size $r_c \approx 500$ nm is weak and even has an opposite sign: $x_{\rm left}$ for 3D-2D in Fig. 8 is more to the left relative to the 1D one; this is caused by thermal fluctuations creating nuclei of voids and their stochastic interactions and coalescence randomly curving the vacuum boundary, see Fig. 7(b). For small r_c of the order of thickness of a film, the 3D effects should decelerate expansion relative to the 1D case (when $r_c = \infty$).

Nevertheless, comparing the 1D 2T-HD and 1D MD velocities $V_{\rm vac}$ in Fig. 9, we see that a spallation plate flies

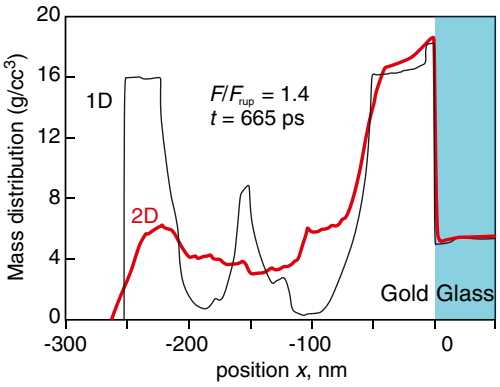

FIG. 8. Comparison of 1D No. 353 (see Table II) and 3D-2D No. 355 expansions in places with equal local values of $F = 1.4F_{\rm rup}$. For the 3D-2D case this is the central zone around the plane $y = y_c$, where y_c is the y coordinate of the tip point. The 3D MD run shown in Fig. 7(b) has a depth in the z direction equal to 8.2 nm. Directions x, y, and z relate to the expansion direction (vertical direction in Fig. 7), horizontal direction in Fig. 7, and to the normal to the plane of picture, respectively. The z depth is small relative to the x, y sizes. Thus, the nucleation and initial expansion of voids start in the 3D environment. But later the foam transits to 2D expansion. Therefore, we call this case the 3D-2D case and write "2D" for the corresponding mass distribution $\langle rho(x)\rangle$ obtained by averaging along the planes $x = \text{const}$. The edge points $x_{\rm left}$ where $\langle\rho(x_{\rm left})\rangle = 0$ for 1D and 2D distributions are approximately the same. This means that the 3D-2D effects (finite size of r_c) weakly influence the dynamics of expansion for $r_c \approx 1000/2 = 500$ nm.

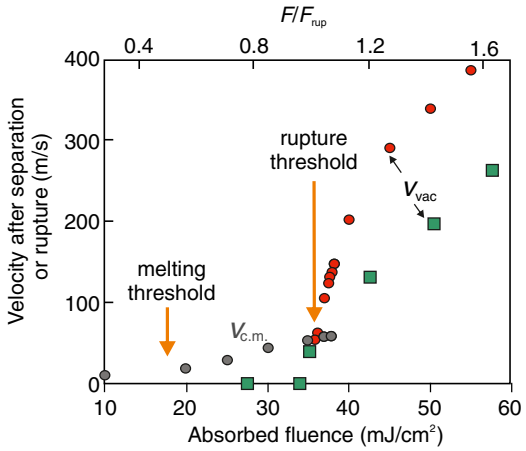

FIG. 9. This is the 1D 2T-HD dependencies taken from Fig. 4 (gray and red filled circles) compared with the six 1D MD runs Nos. 350, 351a, 351, 352, 353, 354 (from Table II) shown by the green filled squares. The snapshot $t = 0.665$ ns of the case No. 353 is presented in Fig. 7(A). These runs are followed up to the stage of rupture of all membranes connecting the contact part of a film and the vacuum part (spallation plate) of a film; see Fig. 4(b). This refers to the last four runs which are above the rupture threshold $F_{\rm rup}$. Their green squares give asymptotic velocities $V_{\rm c.m.\,SP}$ of the center of mass of the spallation plates (SP). Values of $F_{\rm rup}$ for 1D 2T-HD and 1D MD simulations moderately differ, see beginning of Note 4. Therefore, 1D MD velocities $V_{\rm c.m.\,SP}$ (or $V_{\rm vac}$) are shown as the function of normalized fluence $F/F_{\rm rup}$ given at the upper horizontal axis. While the 1D 2T-HD velocities $V_{\rm c.m.}$ and $V_{\rm c.m.\,SP}$ (or $V_{\rm vac}$) depend on absorbed fluence given at the bottom horizontal axis.

TABLE II. Increase of temperature T_{sp} and decrease of thickness of a spallation plate d_{sp} with an increase of absorbed fluence in the six 1D MD runs.

F/F_{rup}	T_{sp} (K)	d_{sp} (nm)	No.
0.783			350
0.957			351a
1	1560	39	351
1.21	1790	40.5	352
1.43	2020	37	353
1.63	2260	34.9	354

faster in hydrodynamics, probably because the deceleration by membranes in foam is absent. Let us mention that the amount of velocity ~60 m/s should be extracted from the 1D 2T-HD spallation velocity $V_{vac}(F_{abs})$ in Fig. 9 because the temporal interval of positive contact pressure doesn't add momentum to the film in the case of large adhesion.

A decreased value of the electron heat conduction coefficient κ is used in 1D and 3D-2D MD simulations shown in Figs. 7–9. Therefore, there is a solid layer of gold near the contact with glass in Fig. 7; solid is green, liquid is red. The narrow layer of glass near the contact is molten thanks to its ion thermal conductivity; we neglect electron conduction in glass. Temperatures T_{sp} and thicknesses of the spallation plates d_{sp} as functions of absorbed energy are given in Table II.

Above, around Figs. 7–9 we have discussed the significance of lateral gradients (applicability of local approximation) and have concluded that for $r_c > 500$ nm they are of small importance. The only place that should be checked in the future relates to matching between the molten spot and solid film outside the spot. Because the simulations from Table I have a narrow transition area outside the bump, which definitely increases the velocity $V_{c.m.}$ necessary to form a jet and thus decreases the distance from an origin to the jet-bump boundary in Fig. 4; here, we worry about the correspondence between theoretical and experimental jet-bump boundaries in Fig. 4.

The simulation shown in Fig. 7(b) doesn't include a cooling thermostat at the left and right lateral edges. Thus, it is difficult to imagine how the experimental situation may look above the threshold F_{rup}.

To be closer to experiment, the simulations box laterally extending around the molten spot is necessary. In our simulations presented in Table I the square simulation box is only 8% (the side of the square is 140 nm while the diameter of the circle is 130 nm) and 4% (270/260) larger than the circle of bump basement.

(i) The thermal sink should be placed far from the edge of the cupola. The sink supports $T = 300$ K. Thus, the melting and recrystallization front is somewhere in between the sink and the center of the hottest spot. Its radius increases quickly during the 2T stage, then for some time increases slowly, and after that begins to decrease at the nanosecond time scale due to the gradually propagating recrystallization front. The distance of the order of the cupola radius from the edge of the cupola is enough for posting of the sink thanks to 2D spatial expansion of the cooling flux along the metal film from the hot spot to the cold peripheral region of the film.

(ii) Another important ingredient is the resistance of a solid film to its bending. This effect alone (even at zero cohesion) defines the value of the threshold for nanobump formation. The mass of a whole film is infinite, thus the finite amount of momentum directed to vacuum and transferred during the acoustic time scale inside an irradiated spot to the film is not enough for significant bumping; bending of the solid film has been considered in Refs. [41,42] for pulse-durations–thickness–film-material 30 fs/40 nm/Au and 30 ns/200 nm/SnO, respectively. To significantly bend a solid film, we have to melt it inside a spot having a rather significant size.

In Ref. [33] the simulation circle is 25 times larger (125 nm versus 5 nm) than the radius of the laser beam equal to $R_L = 5$ nm. Extremely large energy 3.1 J/cm^2 is injected into this laterally very small spot (the thickness of a Ni film is 20 nm). During the time interval t_{eq} (few picoseconds, duration of 2T stage) this energy spreads out radially filling up a spot with the radius of the order of thickness of a heat-affected zone in a bulk Ni target. After the equilibration of electron and ion temperatures, a coefficient of electron heat conduction in Ref. [33] drops down to its value κ_{ref} known from reference books. The value κ_{ref} isn't scaled down as it is described above in Sec. III. Therefore, the situation considered in Ref. [33] corresponds exactly to the case with the radius $R_L = 5$ nm. It cannot be applied to illuminations with optical radiuses R_L of the order of a few hundreds of nanometers and larger; because small-radius R_L and normal-conduction κ_{ref} suppress jet formation—a bump freezes too fast. Indeed, the value κ_{ref} in Ref. [33] is large, thus thermal velocity ν_χ (3) is large for so small R_L. Then the relative thermal number V_κ (2) is large in spite of a huge injected energy 3.1 J/cm^2. In these conditions the bump begins to recrystallize quickly, it does not have time to develop a jet.

There is a common method [71] $(\ln E, R_{opt}^2)$ used to measure the transverse radius R_{opt} of a laser beam, here E is a pulse energy. This procedure is based on the two assumptions: (i) the fixed modification degree of a target depends only on the local absorbed fluence and (ii) the fluence distribution may be approximated by a Gaussian function. However, for our conditions with a very small irradiation spot the first assumption is not accurate.

Let us discuss important data presented in Fig. 1(h) showing the dependence of the geometrical size of the corresponding type of the structure (marked with different colors) on the applied pulse-energy–absorbed fluence. The three colored parts of this dependence fitted with the straight lines have a different slope for fixed focusing

conditions ($R_{opt} = \text{const}$) used in all three fluence ranges, which means that the first assumption made in Ref. [71] is not applicable; there is significant nonlocal influence. Another important point is that the optical beam radius $R_{opt} = 630$ nm estimated using an expression $R_{opt} = 0.61\lambda\,(\mathrm{NA})^{-1}$ differs from the approximate radius of ≈450 nm derived for the bumps and jets in Fig. 1(h) by the common approach [71]. Let us restrict ourselves by discussion of the fluence range required to produce nanobumps and bumps with jets atop. Absorbed fluences are of the order of predicted in our simulations. The experimental bumps in Fig. 1(h) are formed above the threshold equal to ≈20 mJ/cm^2, while in the 1D approximation this value should be equal to 0 in the absence of cohesion. The value of 20 mJ/cm^2 slightly overcomes the melting threshold for our gold film; see Fig. 4. It seems that both the resistance to bending and some possible small cohesion contribute to the corresponding increase of the bumping threshold. Thus, it is not surprising that additional factors increase the thresholds relative to modeling. Therefore, the rupture threshold in Fig. 4(a) is shifted to its possible position in the point $F_{abs} \approx 60$ mJ/cm^2, ≈110 m/s.

[1] R. R. Gattass, L. R. Cerami, and E. Mazur, Micromachining of bulk glass with bursts of femtosecond laser pulses at variable repetition rates, Opt. Express **14**, 5279 (2006).

[2] L. Shah, A. Y. Arai, S. M. Eaton, and P. R. Herman, Waveguide writing in fused silica with a femtosecond fiber laser at 522 nm and 1 MHz repetition rate, Opt. Express **13**, 1999 (2005).

[3] L. Boinovich, A. Domantovskiy, A. Emelyanenko, A. Pashinin, A. Ionin, S. Kudryashov, and P. Saltuganov, Femtosecond laser treatment for the design of electro-insulating superhydrophobic coatings with enhanced wear resistance on glass, ACS Appl. Mater. Interfaces **6**, 2080 (2014).

[4] Z. Qian, A. Covarrubias, A. W. Grindal, M. K. Akens, L. Lilge, and R. S. Marjoribanks, Dynamic absorption and scattering of water and hydrogel during high-repetition-rate (> 100 MHz) burst-mode ultrafast-pulse laser ablation, Biomed. Opt. Express **7**, 2331 (2016).

[5] C. Kerse, H. Kalaycıoğlu, P. Elahi, B. Çetin, D. K. Kesim, Ö. Akçaalan, S. Yavaş, M. D. Aşık, B. Öktem, H. Hoogland, R. Holzwarth, and F. Ö. Ilday, Ablation-cooled material removal with ultrafast bursts of pulses, Nature (London) **537**, 84 (2016).

[6] Y.-C. Wang, J.-M. Shieh, H.-W. Zan, and C.-L. Pan, Near-infrared femtosecond laser crystallized poly-Si thin film transistors, Opt. Express **15**, 6982 (2007).

[7] S. Haas, A. Gordijn, and H. Stiebig, High speed laser processing for monolithical series connection of silicon thin-film modules, Prog. Photovolt: Res. Appl. **16**, 195 (2008).

[8] A. Vorobyev and C. Guo, Direct femtosecond laser surface nano/microstructuring and its applications, Laser Photonics Rev. **7**, 385 (2013).

[9] U. Zywietz, A. B. Evlyukhin, C. Reinhardt, and B. N. Chichkov, Laser printing of silicon nanoparticles with resonant optical electric and magnetic responses, Nat. Commun. **5**, 34022 (2014).

[10] C. W. Visser, R. Pohl, C. Sun, G.-W. Römer, and B. Huis in't Veld, and D. Lohse, Toward 3D printing of pure metals by laser-induced forward transfer, Adv. Mater. **27**, 4087 (2015).

[11] P. A. Dmitriev, S. V. Makarov, V. A. Milichko, I. S. Mukhin, A. S. Gudovskikh, A. A. Sitnikova, A. K. Samusev, A. E. Krasnok, and P. A. Belov, Laser fabrication of crystalline silicon nanoresonators from an amorphous film for low-loss all-dielectric nanophotonics, Nanoscale **8**, 5043 (2016).

[12] A. Kuchmizhak, O. Vitrik, Yu. Kulchin, D. Storozhenko, A. Mayor, A. Mirochnik, S. Makarov, V. Milichko, S. Kudryashov, V. Zhakhovsky, and N. Inogamov, Laser printing of resonant plasmonic nanovoids, Nanoscale **8**, 12352 (2016).

[13] X. W. Wang, A. A. Kuchmizhak, E. Brasselet, and S. Juodkazis, Dielectric geometric phase optical elements from femtosecond direct laser writing, Appl. Phys. Lett. **110**, 181101 (2017).

[14] A. I. Kuznetsov, A. B. Evlyukhin, M. R. Gonçalves, C. Reinhardt, A. Koroleva, M. L. Arnedillo, R. Kiyan, O. Marti, and B. N. Chichkov, Laser fabrication of large-scale nanoparticle arrays for sensing applications, ACS Nano **5**, 4843 (2011).

[15] M. Zenou, A. Sa'ar, and Z. Kotler, Laser transfer of metals and metal alloys for digital microfabrication of 3D objects, Small **11**, 4082 (2015).

[16] R. Fang, A. Vorobyev, and C. Guo, Direct visualization of the complete evolution of femtosecond laser-induced surface structural dynamics of metals, Light Sci. Appl. **6**, e16256 (2017).

[17] S. V. Makarov, M. I. Petrov, U. Zywietz, V. A. Milichko, D. A. Zuev, N. Lopanitsyna, A. Kuksin, I. Mukhin, G. Zograf, E. Ubyivovk, D. Smirnova, S. Starikov, B. N. Chichkov, and Y. S. Kivshar, Efficient second-harmonic generation in nanocrystalline silicon nanoparticle, Nano Lett. **17**, 3047 (2017).

[18] C. Unger, J. Koch, L. Overmeyer, and B. N. Chichkov, Time-resolved studies of femtosecond-laser induced melt dynamics, Opt. Express **20**, 24864 (2012).

[19] A. I. Kuznetsov, C. Unger, J. Koch, and B. N. Chichkov, Laser-induced jet formation and droplet ejection from thin metal films, Appl. Phys. A **106**, 479 (2012).

[20] S. I. Ashitkov, N. A. Inogamov, V. V. Zhakhovskii, Yu. N. Emirov, M. B. Agranat, I. I. Oleinik, S. I. Anisimov, and V. E. Fortov, Formation of nanocavities in the surface layer of an aluminum target irradiated by a femtosecond laser pulse, JETP Lett. **95**, 176 (2012).

[21] J. V. Oboňa, V. Ocelík, J. C. Rao, J. Z. P. Skolski, G. R. B. E. Römer, and A. J. Huis in't Veld, and J. Th. M. De Hosson, Modification of cu surface with picosecond laser pulses, Appl. Surf. Sci. **303**, 118 (2014).

[22] Y. Nakata, N. Miyanaga, K. Momoo, and T. Hiromoto, Solid-liquid-solid process for forming free standing gold nanowhisker superlattice by interfering femtosecond laser irradiation, Appl. Surf. Sci. **274**, 27 (2013).

[23] N. A. Inogamov, V. V. Zhakhovskii, and V. A. Khokhlov, Jet formation in spallation of metal film from substrate under

action of femtosecond laser pulse, J. Exp. Theor. Phys. **120**, 15 (2015).
[24] D. Yuan, R. Acharya, and S. Das, Fabrication of gold nanostructures through pulsed laser interference patterning, Appl. Phys. Lett. **103**, 223101 (2013).
[25] C. Wu, M. S. Christensen, J.-M. Savolainen, P. Balling, and L. V. Zhigilei, Generation of subsurface voids and a nanocrystalline surface layer in femtosecond laser irradiation of a single-crystal Ag target, Phys. Rev. B **91**, 035413 (2015).
[26] D. S. Ivanov, V. P. Lipp, A. Blumenstein, F. Kleinwort, V. P. Veiko, E. Yakovlev, V. Roddatis, M. E. Garcia, B. Rethfeld, J. Ihlemann, and P. Simon, Experimental and Theoretical Investigation of Periodic Nanostructuring of Au with Ultrashort UV Laser Pulses Near the Damage Threshold, Phys. Rev. Applied **4**, 064006 (2015).
[27] D. Shen, G. Zou, L. Liu, W. W. Duley, and Y. N. Zhou, Investigation of splashing phenomena during the impact of molten sub-micron gold droplets on solid surfaces, Soft Matter **12**, 295 (2016).
[28] L. Chen, T. Zhai, X. Zhang, C. Unger, J. Koch, B. N. Chichkov, and P. J. Klar, Polarization-dependent SERS effects of laser-generated sub-100 nm antenna structures, Nanotechnology **25**, 265302 (2014).
[29] C. Wu and L. Zhigiley, Nanocrystalline and polyicosahedral structure of a nanospike generated on metal surface irradiated by a single femtosecond laser pulse, J. Phys. Chem. C **120**, 4438 (2016).
[30] N. A. Inogamov, V. V. Zhakhovsky, and K. P. Migdal, Laser-induced spalling of thin metal film from silica substrate followed by inflation of microbump, Appl. Phys. A **122**, 432 (2016).
[31] M. E. Povarnitsyn, T. E. Itina, M. Sentis, K. V. Khishchenko, and P. R. Levashov, Material decomposition mechanisms in femtosecond laser interactions with metals, Phys. Rev. B **75**, 235414 (2007).
[32] D. S. Ivanov, B. Rethfeld, G. M. O'Connor, T. J. Glynn, A. N. Volkov, and L. V. Zhigilei, The mechanism of nanobump formation in femtosecond pulse laser nanostructuring of thin metal films, Appl. Phys. A **92**, 791 (2008).
[33] D. S. Ivanov, Zh. Lin, B. Rethfeld, G. M. O'Connor, T. J. Glynn, and L. V. Zhigilei, Nanocrystalline structure of nanobump generated by localized photoexcitation of metal film, J. Appl. Phys. **107**, 013519 (2010).
[34] D. S. Ivanov, A. I. Kuznetsov, V. P. Lipp, B. Rethfeld, B. N. Chichkov, M. E. Garcia, and W. Schulz, Short laser pulse nanostructuring of metals: Direct comparison of molecular dynamics modeling and experiment, Appl. Phys. A **111**, 675 (2013).
[35] C. Wu and L. Zhigilei, Microscopic mechanisms of laser spallation and ablation of metal targets from large-scale molecular dynamics simulations, Appl. Phys. A **114**, 11 (2014).
[36] A. Kuchmizhak, E. Pustovalov, S. Syubaev, O. Vitrik, Y. Kulchin, A. Porfirev, S. Khonina, and S. Kudryashov, On-fly femtosecond-laser nanolithographic fabrication of self-organized plasmonic nanotextures for chemo- and biosensing applications, ACS Appl. Mater. Interfaces **8**, 24946 (2016).
[37] S. V. Makarov, A. O. Levchenko, A. A. Rudenko, I. N. Saraeva, D. A. Zayarny, C. R. Nathala, W. Husinsky, A. A. Ionin, and S. I. Kudryashov, Nanoscale surface boiling in sub-threshold damage and above-threshold spallation of bulk aluminum and gold by single femtosecond laser pulses, Laser Phys. Lett. **13**, 025603 (2016).
[38] S. V. Starikov and V. V. Pisarev, Atomistic simulation of laser-pulse surface modification: Predictions of models with various length and time scales, J. Appl. Phys. **117**, 135901,1 (2015).
[39] S. Babar and J. H. Weaver, Optical constants of Cu, Ag, and Au revisited, Appl. Opt. **54**, 477 (2015).
[40] *Handbook of Optical Constants of Solids*, edited by E. D. Palik (Academic Press, New York, 1998).
[41] Y. P. Meshcheryakov, M. V. Shugaev, T. Mattle, T. Lippert, and N. M. Bulgakova, Role of thermal stresses on pulsed laser irradiation of thin films under conditions of microbump formation and nonvaporization forward transfer, Appl. Phys. A **113**, 521 (2013).
[42] Y. P. Meshcheryakov and N. M. Bulgakova, Thermoelastic modeling of microbump and nanojet formation on nanosize gold films under femtosecond laser irradiation, Appl. Phys. A **82**, 363 (2006).
[43] *Handbook of Physical Constants*, edited by A. A. Radzig, I. S. Grigoriev, and E. Z. Meilikhov (CRC Press, Bosa Roca, 1996).
[44] Yu. N. Kulchin, O. B. Vitrik, A. A. Kuchmizhak, A. G. Savchuk, A. A. Nepomnyashchii, P. A. Danilov, D. A. Zayarnyi, A. A. Ionin, S. I. Kudryashov, S. V. Makarov, A. A. Rudenko, V. I. Yurovskikh, and A. A. Samokhin, Formation of nanobumps and nanoholes in thin metal films by strongly focused nanosecond laser pulses, J. Exp. Theor. Phys. **119**, 15 (2014).
[45] P. A. Danilov, D. A. Zayarnyi, A. A. Ionin, S. I. Kudryashov, S. V. Makarov, A. A. Rudenko, V. I. Yurovskikh, Yu. N. Kulchin, O. B. Vitrik, A. A. Kuchmizhak, E. A. Drozdova, and S. B. Odinokov, Mechanisms of formation of sub- and micrometre-scale holes in thin metal films by single nano- and femtosecond laser pulses, Quantum Electron. **44**, 540 (2014).
[46] N. A. Inogamov, V. V. Zhakhovsky, A. Y. Faenov, V. A. Khokhlov, V. V. Shepelev, I. Y. Skobelev, Y. Kato, M. Tanaka, T. A. Pikuz, M. Kishimoto, M. Ishino, M. Nishikino, Y. Fukuda, S. V. Bulanov, T. Kawachi, Yu. V. Petrov, S. I. Anisimov, and V. E. Fortov, Spallative ablation of dielectrics by x-ray laser, Appl. Phys. A **101**, 87 (2010).
[47] E. T. Karim, M. V. Shugaev, C. Wu, Z. Lin, H. Matsumoto, M. Conneran, J. Kleinert, R. F. Hainsey, and L. V. Zhigilei, Experimental characterization and atomistic modeling of interfacial void formation and detachment in short pulse laser processing of metal surfaces covered by solid transparent overlayers, Appl. Phys. A **122**, 407 (2016).
[48] N. A. Inogamov, V. V. Zhakhovsky, V. A. Khokhlov, S. I. Ashitkov, Y. N. Emirov, K. V. Khichshenko, A. Ya. Faenov, T. A. Pikuz, M. Ishino, M. Kando, N. Hasegawa, M. Nishikino, P. S. Komarov, B. J. Demaske, M. B. Agranat, S. I. Anisimov, T. Kawachi, and I. I. Oleynik, Ultrafast lasers and solids in highly excited states: Results of hydrodynamics and molecular dynamics simulations, J. Phys. Conf. Ser. **510**, 012041 (2014).
[49] D. K. Ilnitskiy, V. A. Khokhlov, V. V. Zhakhovsky, Yu. V. Petrov, K. P. Migdal, and N. A. Inogamov, Dynamics of

laser ablation at the early stage during and after ultrashort pulse, J. Phys. Conf. Ser. **774**, 012101 (2016).
[50] S. Amoruso, N. N. Nedyalkov, X. Wang, G. Ausanio, R. Bruzzese, and P. A. Atanasov, Ultrafast laser ablation of gold thin film targets, J. Appl. Phys. **110**, 124303 (2011).
[51] S. Amoruso, N. N. Nedyalkov, X. Wang, G. Ausanio, R. Bruzzese, and P. A. Atanasov, Ultrashort-pulse laser ablation of gold thin film targets: Theory and experiment, Thin Solid Films **550**, 190 (2014).
[52] V. V. Zhakhovskii, N. A. Inogamov, Yu. V. Petrov, S. I. Ashitkov, and K. Nishihara, Molecular dynamics simulation of femtosecond ablation and spallation with different interatomic potentials, Appl. Surf. Sci. **255**, 9592 (2009).
[53] N. A. Inogamov, V. V. Zhakhovsky, V. A. Khokhlov, A. A. Kuchmizhak, and S. I. Kudryashov, Blistering of film from substrate after action of ultrashort laser pulse, J. Phys. Conf. Ser. **774**, 012102 (2016).
[54] M. Malinauskas, A. Žukauskas, S. Hasegawa, Y. Hayasaki, V. Mizeikis, R. Buividas, and S. Juodkazis, Ultrafast laser processing of materials: From science to industry, Light Sci. Appl. **5**, e16133 (2016).
[55] K. Toyoda, F. Takahashi, S. Takizawa, Yu. Tokizane, K. Miyamoto, R. Morita, and T. Omatsu, Transfer of Light Helicity to Nanostructures, Phys. Rev. Lett. **110**, 143603 (2013).
[56] M. G. Rahimian, F. Bouchard, H. Al-Khazraji, E. Karimi, P. B. Corkum, and V. R. Bhardwaj, Polarization dependent nanostructuring of silicon with femtosecond vortex pulse, APL Photonics **2**, 086104 (2017).
[57] S. Syubaev, A. Zhizhchenko, A. Kuchmizhak, A. Porfirev, E. Pustovalov, O. Vitrik, Yu. Kulchin, S. Khonina, and S. Kudryashov, Direct laser printing of chiral plasmonic nanojets by vortex beams, Opt. Express **25**, 10214 (2017).
[58] J. J. Nivas, F. Cardano, Z. Song, A. Rubano, R. Fittipaldi, A. Vecchione, D. Paparo, L. Marrucci, R. Bruzzese, and S. Amoruso, Surface structuring with polarization-singular femtosecond laser beams generated by a *q*-plate, Sci. Rep. **7**, 42142 (2017).
[59] E. Skoulas, A. Manousaki, C. Fotakis, and E. Stratakis, Biomimetic surface structuring using cylindrical vector femtosecond laser beams, Sci. Rep. **7**, 45114 (2017).
[60] A. Vailionis, E. G. Gamaly, V. Mizeikis, W. Yang, A. Rode, and S. Juodkazis, Evidence of super-dense aluminum synthesized by ultra-fast micro-explosion, Nat. Commun. **2**, 445 (2011).
[61] L. Rapp, B. Haber, C. J. Pickard, J. E. Bradby, E. G. Gamaly, J. S. Williams, and A. V. Rode, Experimental evidence of new tetragonal polymorphs of silicon formed through ultrafast laser-induced confined microexplosion, Nat. Commun. **6**, 7555 (2015).
[62] M. Hase, P. Fons, K. Mitrofanov, A. V. Kolobov, and J. Tominaga, Femtosecond structural transformation of phase-change materials far from equilibrium monitored by coherent phonons, Nat. Commun. **6**, 8367 (2015).
[63] E. Matsubara, S. Okada, T. Ichitsubo, T. Kawaguchi, A. Hirata, P. F. Guan, K. Tokuda, K. Tanimura, T. Matsunaga, M. W. Chen, and N. Yamada, Initial Atomic Motion Immediately Following Femtosecond-Laser Excitation in Phase-Change Materials, Phys. Rev. Lett. **117**, 135501 (2016).
[64] L. Zhong, J. Wang, H. Sheng, Z. Zhang, and S. X. Mao, Formation of monatomic metallic glasses through ultrafast liquid quenching, Nature (London) **512**, 177 (2014).
[65] V. A. Khokhlov, V. V. Zhakhovsky, K. V. Khishchenko, N. A. Inogamov, and S. I. Anisimov, Metal film on substrate: dynamics under action of ultra-short laser pulse, J. Phys. Conf. Ser. **774**, 012100 (2016).
[66] B. J. Demaske, V. V. Zhakhovsky, N. A. Inogamov, and I. I. Oleynik, Ablation and spallation of gold films irradiated by ultrashort laser pulses, Phys. Rev. B **82**, 064113 (2010).
[67] A. K. Upadhyay, N. A. Inogamov, B. Rethfeld, and H. M. Urbassek, Ablation by ultrashort laser pulses: Atomistic and thermodynamic analysis of the processes at the ablation threshold, Phys. Rev. B **78**, 045437 (2008).
[68] N. A. Inogamov, V. V. Zhakhovskii, S. I. Ashitkov, V. A. Khokhlov, Yu. V. Petrov, P. S. Komarov, M. B. Agranat, S. I. Anisimov, and K. Nishihara, Two-temperature relaxation and melting after absorption of femtosecond laser pulse, Appl. Surf. Sci. **255**, 9712 (2009).
[69] W.-L. Chan, R. S. Averback, and D. G. Cahill, Nonlinear energy absorption of femtosecond laser pulses in noble metals, Appl. Phys. A **97**, 287 (2009).
[70] N. A. Inogamov, V. V. Zhakhovsky, and V. A. Khokhlov, in *Proceedings of the Progress In Electromagnetics Research Symposium (PIERS)*, Prague, Czech Republic, 2015 [http://piers.org/piersproceedings/piers2015PragueProc.php], pp. 2413–2417.
[71] J. M. Liu, Simple technique for measurements of pulsed Gaussian-beam spot sizes, Opt. Lett. **7**, 196 (1982).